Supplementary Material

Vacancy Controlled Nanoscale Cation Ordering Leads to High Thermoelectric Performance

Riddhimoy Pathak[1,†], Lin Xie[2,†], Subarna Das[1], Tanmoy Ghosh[1], Animesh Bhui[1], Kapildeb Dolui[3], Dirtha Sanyal[4], Jiaqing He[2] and Kanishka Biswas[1,*]

[1]New Chemistry Unit, International Centre for Materials Science and School of Advanced Materials, Jawaharlal Nehru Centre for Advanced Scientific Research (JNCASR), Jakkur P.O., Bangalore, 560064, India.

[2]Department of Physics, Southern University of Science and Technology, Shenzhen, 518055, China,

[3]Department of Materials Science & Metallurgy, University of Cambridge, 27 Charles Babbage Road, Cambridge CB3 0FS, United Kingdom

[4]Variable Energy Cyclotron Centre, 1A/F Bidhannagar, Kolkata 700064, India

[†]These authors contributed equally to this work

[*]Corresponding author- kanishka@jncasr.ac.in

Methods

Reagents. Silver (Ag, Strategy Elements, 99.999 %), tellurium (Te, Strategy Elements, 99.99 %) and antimony (Sb, Alfa Aesar, 99.999 %) were used for synthesis of all the compounds.

Synthesis. High-quality crystalline ingots (~8 g) of $Ag_{1-x}SbTe_2$ (x=0, 0.01, 0.02 and 0.03) were synthesized by mixing appropriate ratios of high purity starting materials of Ag, Sb, and Te in a quartz tube with diameter of 10 mm. The tubes were sealed under vacuum (10^{-6} Torr) and slowly heated to 673 K over 12 h, then heated up to 1123 K in 4 h, annealed for 10 h and then slowly cool down to room temperature over a period of 20 h. The ingots were further annealed at 573 K for 6 h to ensure homogenisation of the material.

Powder X-ray diffraction (PXRD). Room temperature powder X-ray diffraction (PXRD) patterns for all the samples ($Ag_{1-x}SbTe_2$ where x=0, 0.01, 0.02 and 0.03) were recorded in a Rigaku Smartlab SE diffractometer using Cu Kα radiation (λ=1.5406 Å).

Differential scanning calorimetry (DSC). A METTLER-TOLEDO differential scanning calorimeter was used to collet DSC data with a ramp rate of 2 K/min in nitrogen atmosphere.

Transmission electron microscopy. Transmission electron microscopy (TEM) samples were prepared by conventional mechanical and tripod polishing. Large electron transport area was obtained by subsequent Ar ion milling in the precision ion polishing system (PIPS) with the ion energy of 4 eV and beam angle of 7 deg. The thickness was restricted to 80-90 μm. TEM experiment was carried out using an aberration corrected Thermo Fisher Themis 60-300 keV transmission electron microscope operating at 300 keV. The convergence angle and the collection angle for STEM imaging are 25 mrad and 63–200 mrad, respectively. The sample drift and signal-to-noise ratio was improved by acquiring a series of images sequentially with a dwell time of 0.5 μs for each pixel. After the acquisition, the images were aligned frame by frame using the commercial software Velox and then summed together to obtain a single image.

Thermal conductivity. Thermal diffusivity, D, of the samples was measured by laser flash diffusivity method using a Netzsch LFA-457 in the 300−573 K temperature range under N_2 atmosphere. Coins with dimensions of ~10 mm diameter and less than ~2 mm thickness were used for the measurements. Temperature dependent heat capacity, C_p, of $AgSbTe_2$ was determined by comparing with a standard sample (pyroceram) in LFA-457 [1]. The total thermal conductivity, κ_{tot}, was then estimated using the formula $\kappa_{tot} = D\rho C_p$, where ρ is the density of the samples which were found to be ~ 97% of the theoretical value.

Minimum lattice thermal conductivity calculations. We have calculated the theoretical minimum lattice thermal conductivity of AgSbTe$_2$ via the Cahill's model [2] (κ_{min}) where:

$$\kappa_{min} = 1.21n^{\frac{2}{3}}k_B\frac{1}{3}(2v_T + v_L) \qquad \text{Eq. 1}$$

where k_B is the Boltzmann constant, and v_T and v_L are the transverse and longitudinal sound velocities respectively, and n represents the number density of atoms. The obtained lattice thermal conductivity of Ag$_{0.98}$SbTe$_2$ was even lesser than the Cahill limit but can be well explained through the diffuson limit (κ_{diff}) which takes into account the atomic vibrations that carry heat through diffusion [3]. It is estimated that:

$$\kappa_{diff} = 0.76n^{\frac{2}{3}}k_B\frac{1}{3}(2v_T + v_L) \qquad \text{Eq. 2}$$

Electrical transport. Electrical conductivity and Seebeck coefficient were measured simultaneously under He atmosphere from room temperature to 573 K using a ULVAC-RIKO ZEM-3 instrument system. The typical sample for measurement had a parallelepiped shape with dimensions of ~2×2×8 mm^3. Low temperature electronic transport (2-300 K) has been measured in DynaCool Physical Property Measurement System (PPMS) [Quantum Design, USA].

Carrier concentration and mobility. AgSbTe$_2$ is a semimetal and a close observation of its electronic band structure reveals dispersive conduction bands and nearly flat valence bands near the Fermi level. Therefore, both electron and hole contribute to the electrical and thermoelectric transport in Ag$_{1-x}$SbTe$_2$ (x=0,0.02) and we estimated their concentration and mobility as described below. Longitudinal magnetoresistance $\rho_{xx}(H)$ and Hall resistance $\rho_{xy}(H)$ of the samples were measured in the temperature range 2-300 K using a DynaCool Physical Property Measurement System (PPMS) [Quantum Design, USA]. Data was taken in the magnetic field range of $\pm$1T after achieving thermal stabilization at each temperature. We fit the experimentally measured $\rho_{xx}(H)$ and $\rho_{xy}(H)$ simultaneously using a two carrier model (Eq S3 and S4) [1,4] to obtain the electron (n) and hole (p) concentrations, and electron (μ_n) and hole (μ_p) mobilities:

$$\frac{\Delta\rho}{\rho} = \frac{\rho_{xx}(H)}{\rho_{xx}(0)} - 1 = AH^2 + CH^4 \qquad \text{Eq. 3}$$

and

$$\rho_{xy}(H) = \frac{1}{e}\left[\frac{-n\mu_n^2 + p\mu_p^2}{(n\mu_n + p\mu_p)^2}H + DH^3\right] \qquad \text{Eq. 4}$$

where,

$$A = \frac{(n\mu_n + p\mu_p)(n\mu_n^3 + p\mu_p^3) - (-n\mu_n^2 + p\mu_p^2)^2}{(n\mu_n + p\mu_p)^2}$$

$$C = \frac{-(n\mu_n + p\mu_p)(n\mu_n^5 + p\mu_p^5) - (n\mu_n^3 + p\mu_p^3)^2 + 2(-n\mu_n^2 + p\mu_p^2)}{(n\mu_n + p\mu_p)^2}$$
$$- \frac{n\mu_n p\mu_p(\mu_n + \mu_p)^2[(-n\mu_n^2 + p\mu_p^2) - 2(n\mu_n + p\mu_p)(n\mu_n^3 + p\mu_p^3)]}{(n\mu_n + p\mu_p)^4}$$

$$D = -\frac{-n\mu_n^4 + p\mu_p^4}{(n\mu_n + p\mu_p)^2} - \frac{(-n\mu_n^2 + p\mu_p^2)[(-n\mu_n^2 + p\mu_p^2)^2 - 2(n\mu_n + p\mu_p)(n\mu_n^3 + p\mu_p^3)]}{(n\mu_n + p\mu_p)^4}$$

Low temperature heat capacity measurement. Specific heat capacity (C_p) at low temperatures (2 – 32 K) of AgSbTe$_2$ and Ag$_{0.98}$SbTe$_2$ was measured using a Quantum Design DynaCool Physical Property Measurement System (PPMS). We fit the low temperature heat capacity data with a combination of Debye and Einstein model [5] as follows:

$$\frac{C_p}{T} = \gamma + \beta T^2 + \sum_n \left(A_n(\theta_{E_n})^2 \cdot (T^2)^{-\frac{3}{2}} \cdot \frac{e^{\frac{\theta_{E_n}}{T}}}{\left(e^{\frac{\theta_{E_n}}{T}} - 1\right)^2} \right) \qquad \text{Eq. 5}$$

where, γ is the Sommerfeld factor which represents the electronic contribution to heat capacity. The second term represents the lattice contribution within Debye theory which are essentially the acoustic phonon modes contributions to the heat capacity. $\beta = B(12\pi^4 N_A k_B/5)(\Theta_D)^{-3}$ where Θ_D, k_B and N_A corresponds to Debye temperature, Boltzmann constant and Avogadro's number respectively and $B = 1 - \sum_n A_n/3NR$ (R: universal gas constant and N: the number of atoms per formula unit). The third term of the equation corresponds to the contributions of the Einstein oscillator modes to the heat capacity in which A_n is the prefactor of the nth Einstein mode and Θ_{En} is the Einstein temperature of the corresponding mode.

Positron annihilation lifetime (PAL) spectroscopy. The positron lifetime measurement has been carried out with a gamma-gamma coincidence technique. A 2.5 cm × 2.5 cm ultra-fast

BaF$_2$ scintillator optically coupled with a XP 2020Q photomultiplier tube is used as a gamma detector [6, 7]. The time resolution of the present fast-fast coincidence setup is 220 ps measured with a ^{60}Co source with the proper positron window. A 10 μCi ^{22}NaCl positron emitting source, covered with a 6-micron thick mylar foil, has been used for the entire positron annihilation experiments. For a typical positron lifetime spectrum, about 10^7 coincidence counts have been recorded and deconvoluted with the PATFIT 88 software [8] with proper source correction. The coincidence Doppler broadening (CDB) spectroscopy has been done with two identical (efficiency ~ 12%; type, PGC 1216sp of DSG) HPGe detectors having energy resolution of about 1.2 keV at 514 keV of ^{85}Sr. The CDB data has been recorded in a dual ADC-based multiparameter data acquisition system, MPA-3 of FAST ComTec. The CDB spectra with ± ΔE selection, ensures a very high peak to background ratio (10^5 : 1). The CDB spectra has been analyzed by constructing the area normalized ratio curve with a pure 99.9999 % Al single crystal.

Lorenz number calculations. The electronic thermal conductivity (κ_e) of Ag$_{1-x}$SbTe$_2$ (x = 0-0.03) was estimated by the Weidemaan-Franz Law: κ_e = LσT where L is the Lorenz number, σ is the electrical conductivity at temperature T. L was estimated by fitting the reduced chemical potential obtained from the temperature dependent Seebeck coefficient using the single parabolic band conduction and assuming dominant acoustic phonon scattering [9]:

$$S = \frac{k_B}{e}\left(\frac{2F_1(\eta)}{F_0(\eta)} - \eta\right) \qquad \text{Eq. 6}$$

and

$$L = \left(\frac{k_B}{e}\right)^2 \frac{3F_0(\eta)F_2(\eta) - 4F_1^2(\eta)}{F_0^2(\eta)} \qquad \text{Eq. 7}$$

where $\eta = (E_F/K_BT)$ in which K$_B$ being the Boltzmaan's constant and the Fermi integral, $F_n(\eta)$ is denoted by:

$$F_n(\eta) = \int_0^\infty \frac{\varepsilon^n}{1+e^{\varepsilon-\eta}} \qquad \text{Eq. 8}$$

The obtained κ_e (Fig. 6b) of Ag$_{1-x}$SbTe$_2$ (x = 0-0.03) was then subtracted from κ_{tot} to obtain the lattice thermal conductivity.

Sound velocity measurement. The longitudinal (ν_l) and transverse (ν_t) sound velocities were measured on a disc-shaped sample by using an Epoch 650 Ultrasonic Flaw Detector (Olympus) instrument with the transducer frequency of 5 MHz. The mean sound velocity (ν_m) was estimated using the formula: $v_m = (\frac{3}{v_l^{-3}+2v_t^{-3}})^{\frac{1}{3}}$ where ν_l and ν_t are longitudinal and transverse sound velocity respectively.

Theoretical calculations of electronic structure. The electronic band structure and formation energy of $AgSbTe_2$ are calculated within the framework of density functional theory (DFT) using generalized gradient approximation (GGA) of the Perdew-Burke-Ernzerhof (PBE) [10] form for the exchange-correlation functional as implemented in the Vinea Ab-initio Simulation Package (VASP). The projector augmented wave (PAW) [11] pseudo-potentials are used to describe the core electrons. Electronic wave-functions are expanded using plane waves up to a cut-off energy of 600 eV. We have considered the AFIIb ordered structure of $AgSbTe_2$ (space group Fd-$3m$)[12] with 16 atoms in the FCC primitive unit cell and 64 atoms in the conventional cubic unit cell. Disorder in the AFIIb structure was introduced by exchanging a pair of Ag and Sb atoms (cations) at the first and second nearest neighbour sites in the 64 atoms cell [13] out of which the latter was more energetically favourable which is similar to the previous reports. Ag vacancy is created by removing an Ag atom at the disordered Ag-site of the conventional unit cell. The Monkhorst-Pack k-mesh is set to $6 \times 6 \times 6$ in the Brillouin zone for the self-consistent calculations, and all atoms are relaxed in each optimization cycle until atomic forces on each atom are smaller than 0.02 eV/°A. The formation energy (E_{form}) is calculated from the energy difference between the material and isolated atoms per conventional unit cell, which is defined as $E_{form} = E_{AgSbTe2} - n_1E_{Ag} - n_2E_{Sb} - n_3E_{Te}$, where E_{tot} is the total energy of the system; E_{Ag}, E_{Sb} and E_{Te} are the total energies per Ag, Sb, and Te atom, respectively in their respective bulk form; and n_1, n_2 and n_3 are the total number of Ag, Sb and Te atoms, respectively in the conventional unit cell. Electronic band structure was calculated for NN-2 disordered $AgSbTe_2$ and $Ag_{0.06}SbTe_2$ after full structural relaxation.

Thermoelectric device fabrication. Fabrication of the double leg thermoelectric device involves consolidation of the $Ag_{0.98}SbTe_2$ powder along with the end layers of Cu/Fe using SPS at 573 K with 50 Mpa for 5 min under vacuum to form the p-type leg. The n-type leg was prepared by sintering $Bi_{0.7}Sb_{0.3}Se$ [14] powder along with the end layers of Cu/Fe using SPS at 573 K with 45 Mpa for 5 min under vacuum. The legs were cut in an appropriate dimension ~4.05x2.55x3.19 mm^3 and 4.05x2.83x2.08 mm^3 for n-type and p-type legs respectively. The

legs are then bonded to 1 mm thick alumina base plate with Cu interconnects. Both the legs are connected to Cu plate by a silver based epoxy layer. Power generating properties of the fabricated device was estimated using a mini-PEM module testing system (Advance Riko) [1, 15]. Output power (P) of the fabricated double-leg device was divided with the total cross-sectional area of the legs to obtain the power density (P_D). However, Mini-PEM module does not offer proper shield to control the radiative heat loss, hence the heat flow through the device is substantially overestimated. Thus, the total amount of heat flow (Q_c) was estimated using the Fourier Law [1, 16] which can be written as:

$$Q_C = \frac{\kappa_{eff}(T_{avg}) * A * \Delta T}{L} \qquad \text{Eq. 9}$$

where A is the total cross-sectional area and L is the length of the fabricated double-leg device. In addition, $\kappa_{eff}(T_{avg})$ is the effective thermal conductivity of the double leg device at $T_{avg} = (T_h + T_c)/2$, and $\Delta T = T_h - T_c$ where T_h and T_c are the temperatures at the hot and cold end respectively. The effective thermal conductivity can be written as:

$$\kappa_{eff} = \frac{(k_1 A_1 + k_2 A_2)}{(A_1 + A_2)} \qquad \text{Eq. 10}$$

Where k_1, k_2 are the thermal conductivity of p-type and n-type leg material at T_{avg} respectively and A_1 and A_2 are the cross-sectional area of the p-type and n-type legs respectively.

Then, the thermoelectric power efficiency (η) was estimated by dividing the total power with the estimated Q_c.
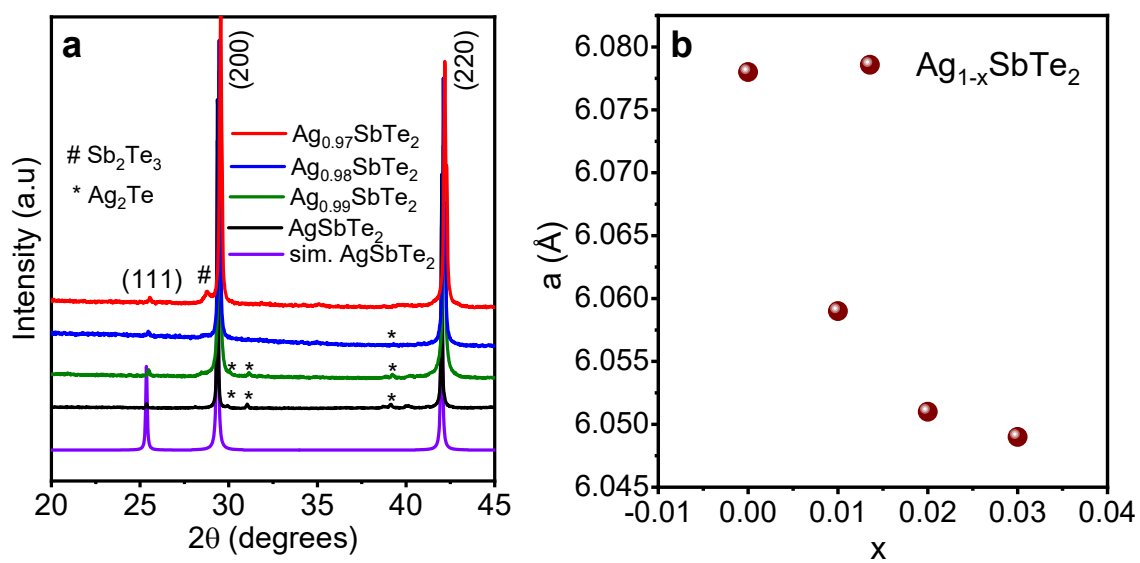
Fig. S1 (a) Room temperature powder X-ray diffraction (XRD) pattern and (b) variation of lattice parameter of $Ag_{1-x}SbTe_2$ (x = 0-0.03).
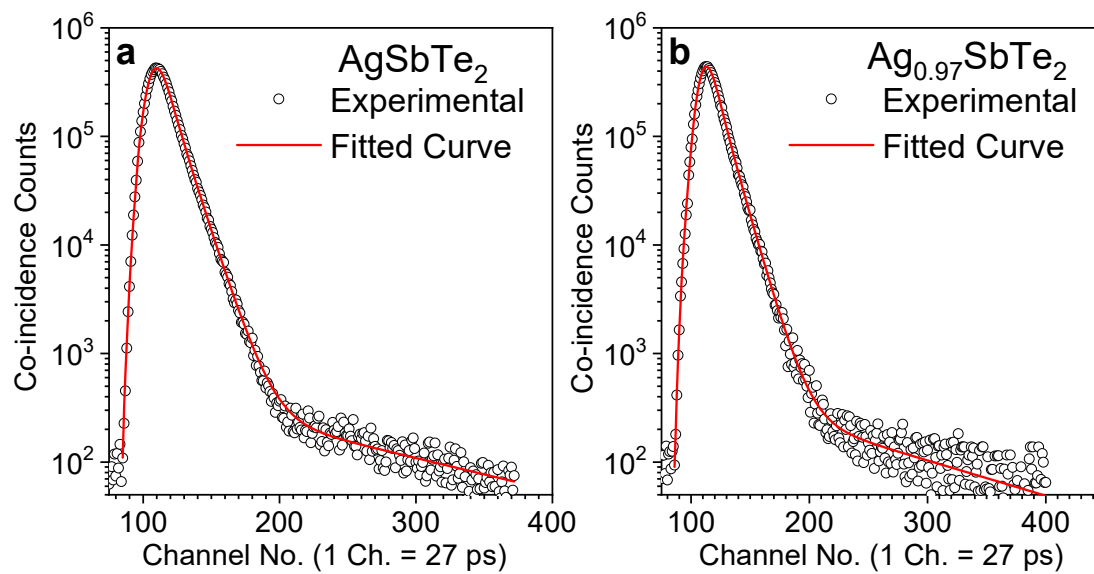
Fig. S2 Positron annihilation lifetime plot of (a) AgSbTe$_2$ and (b) Ag$_{0.97}$SbTe$_2$.
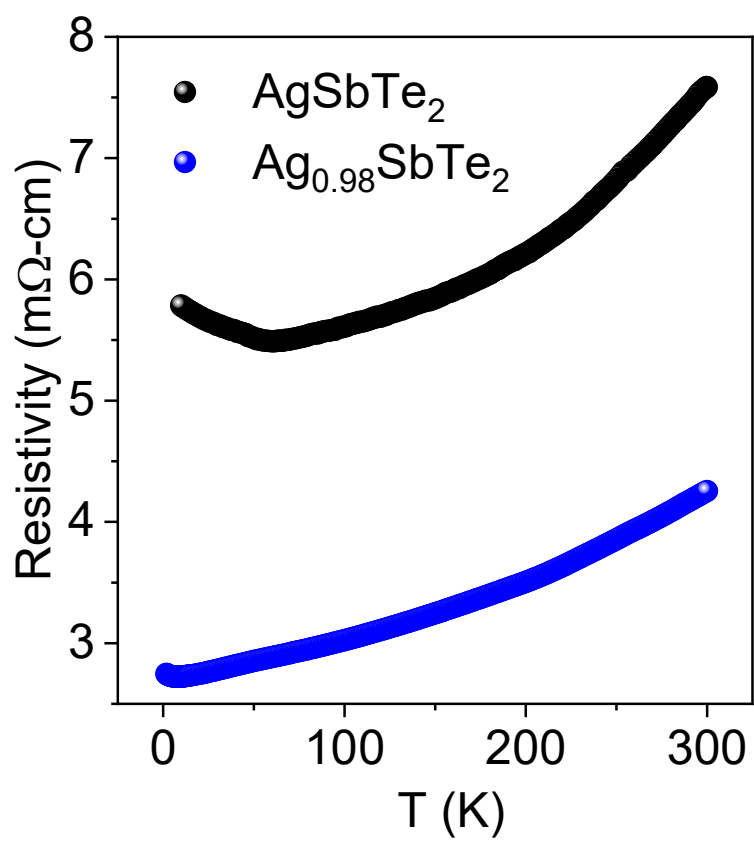
Fig. S3 Temperature variation of electrical resistivity of AgSbTe$_2$ and Ag$_{0.98}$SbTe$_2$.
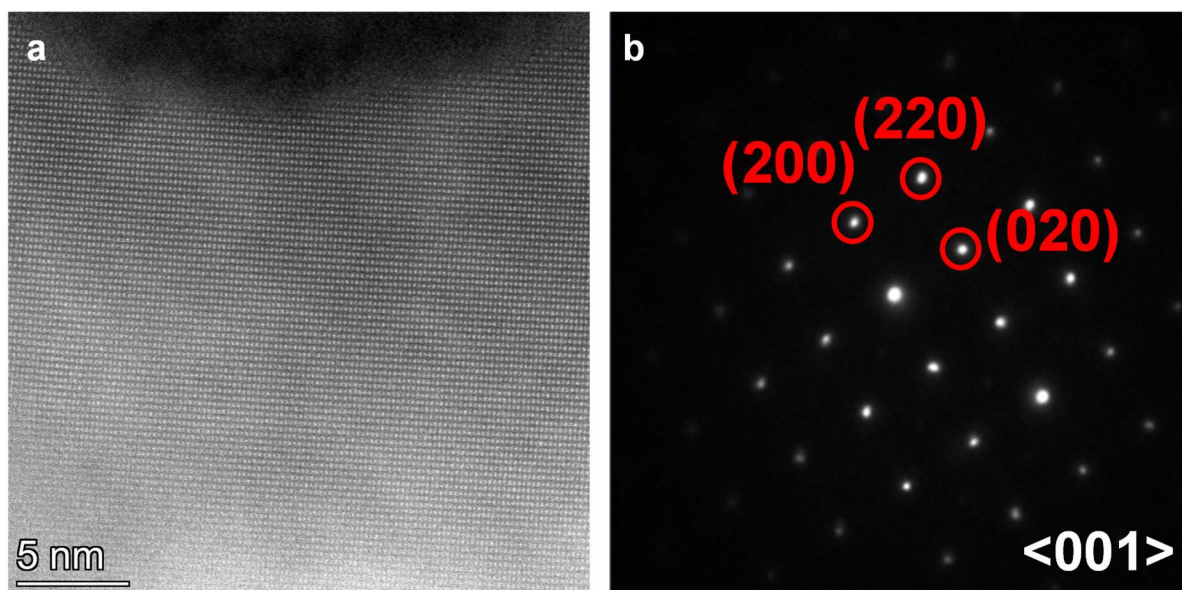
Fig. S4 (a) Atomic-resolution STEM-HAADF and (b) Selected-area electron diffraction pattern of AgSbTe$_2$.
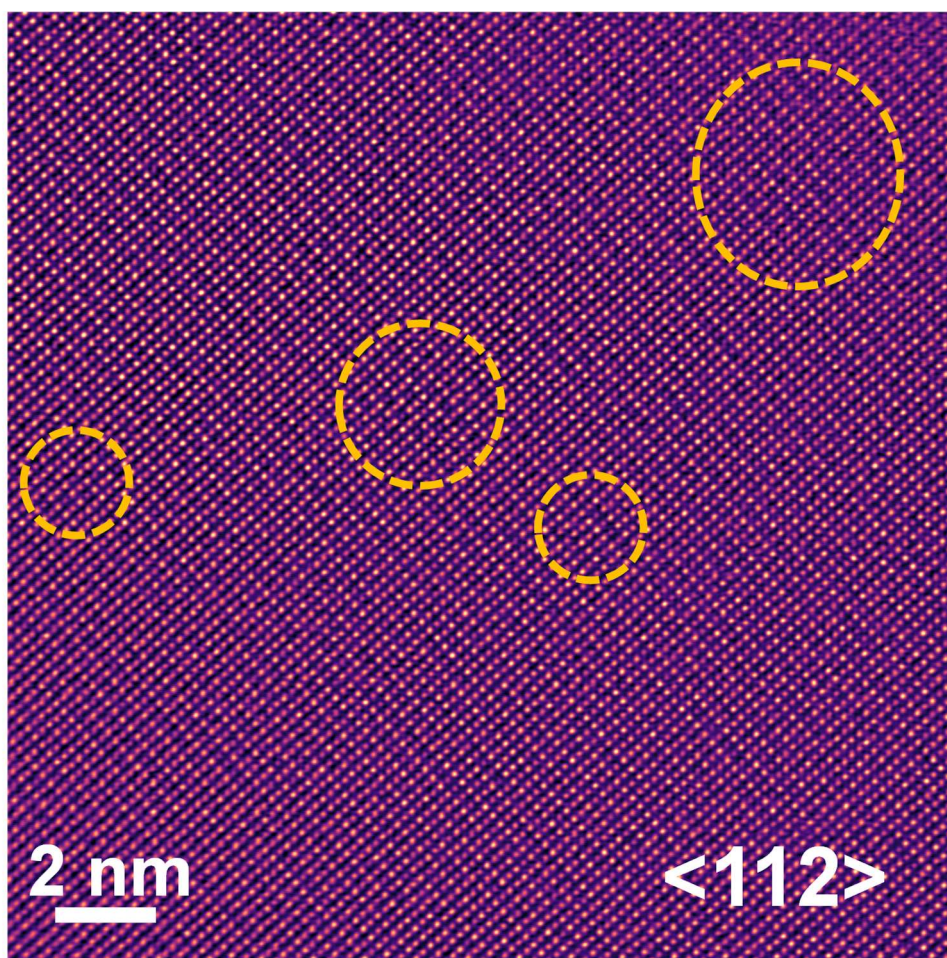
Fig. S5 Singular value decomposition of atomic resolution STEM-HAADF image of $Ag_{0.98}SbTe_2$ showing cation ordered region in yellow circles.
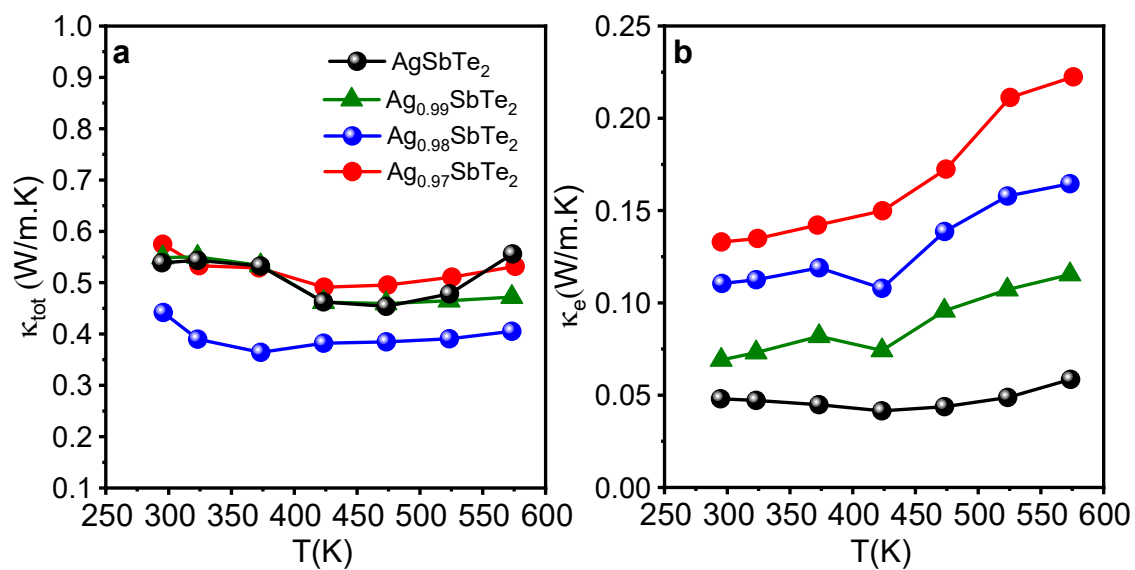
Fig. S6 Temperature variation of (a) total thermal conductivity (κ_{tot}) and (b) electronic thermal conductivity (κ_e) of $Ag_{1-x}SbTe_2$ (x= 0-0.03).
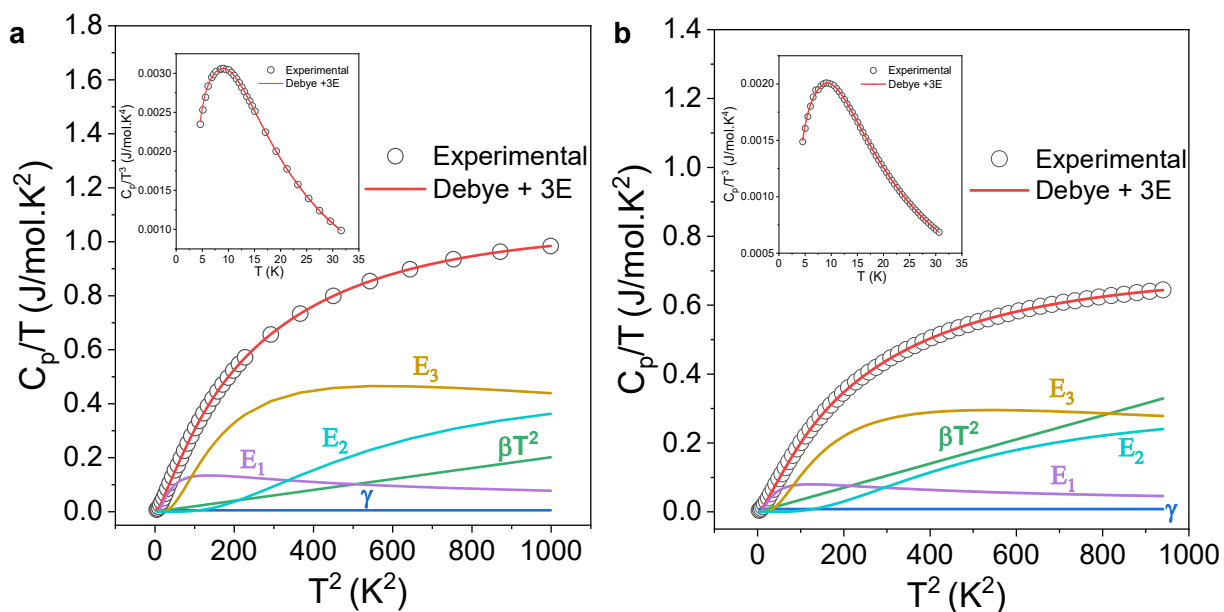
Fig. S7 C_p/T vs. T^2 plot and fit with Debye-Einstein model of (a) AgSbTe$_2$ and (b) Ag$_{0.98}$SbTe$_2$. Individual contributions from electronic (γ), Debye (β) and three Einstein modes (E1, E2 and E3) are also shown in the figures. C_p/T^3 vs. T plot of AgSbTe$_2$ and Ag$_{0.98}$SbTe$_2$ exhibiting a Boson-like peak in the inset of (a) and (b), respectively.
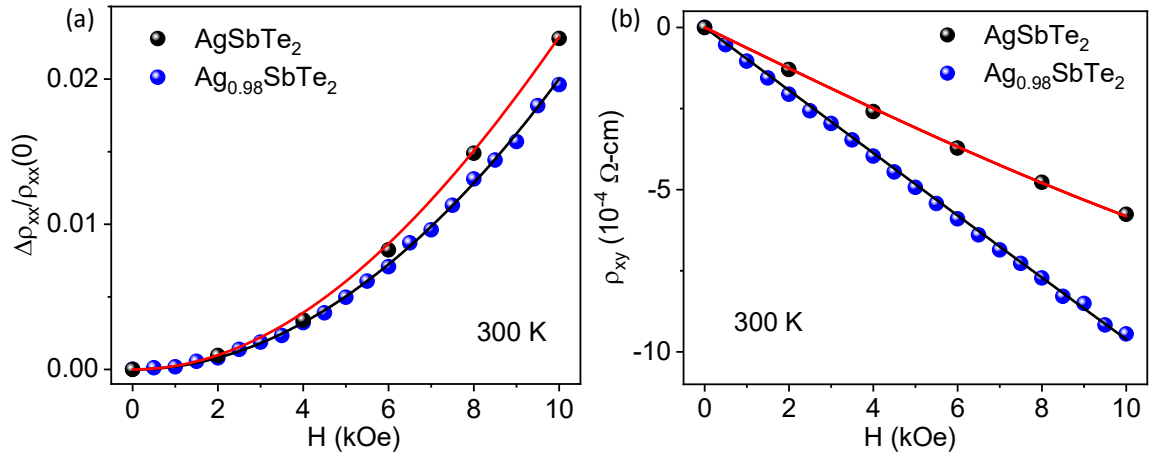
Fig. S8 (a) Magnetoresistance and (b) Hall resistance of $AgSbTe_2$ and $Ag_{0.98}SbTe_2$ (the red and black line indicate the two band model fitting to $AgSbTe_2$ and $Ag_{0.98}SbTe_2$ data respectively).
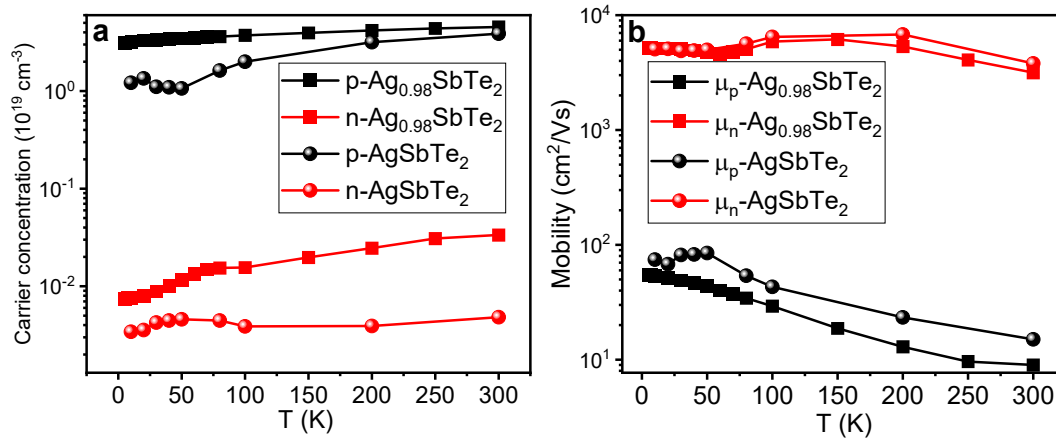
Fig. S9 Temperature variation of (a) carrier concentration and (b) carrier mobility for both p- and n-type carriers in $AgSbTe_2$ and $Ag_{0.98}SbTe_2$ as estimated using two carrier model (Eq 3 and 4) from the magnetoresistance and Hall measurements.
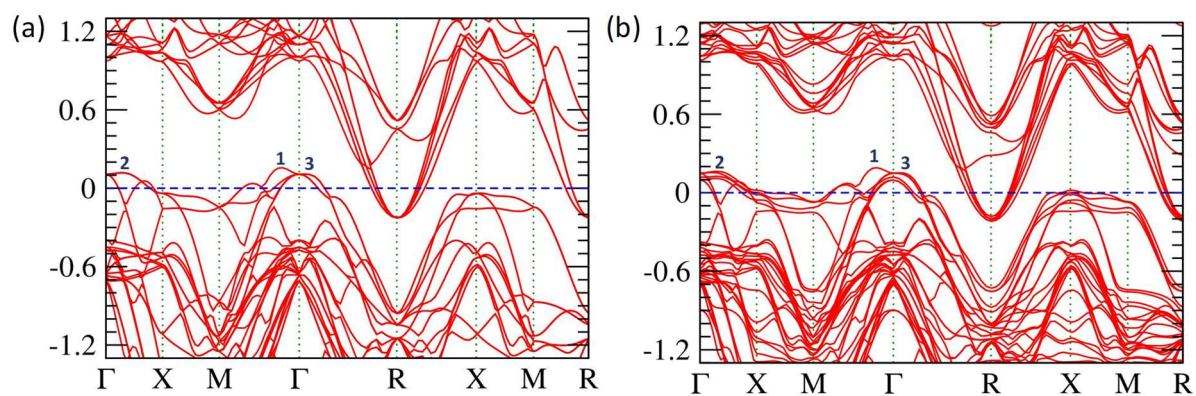
Fig. S10 Electronic band structure of (a) ordered AgSbTe$_2$ and (b) 6 mol% Ag vacant ordered AgSbTe$_2$. 1, 2 and 3 indicate first (VB1), second (VB2), and third valence band (VB3) maxima respectively.
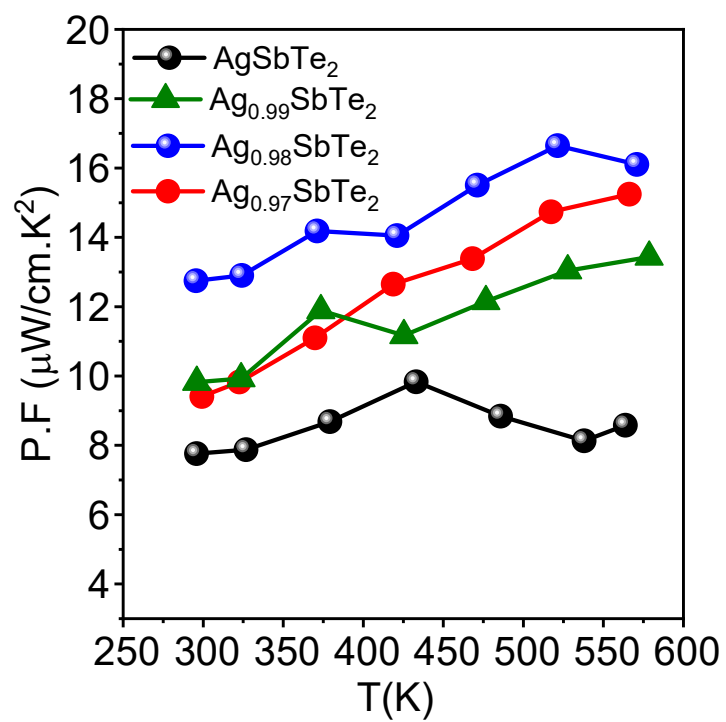
Fig. S11 Temperature variation of power factor of $Ag_{1-x}SbTe_2$ (x= 0-0.03).
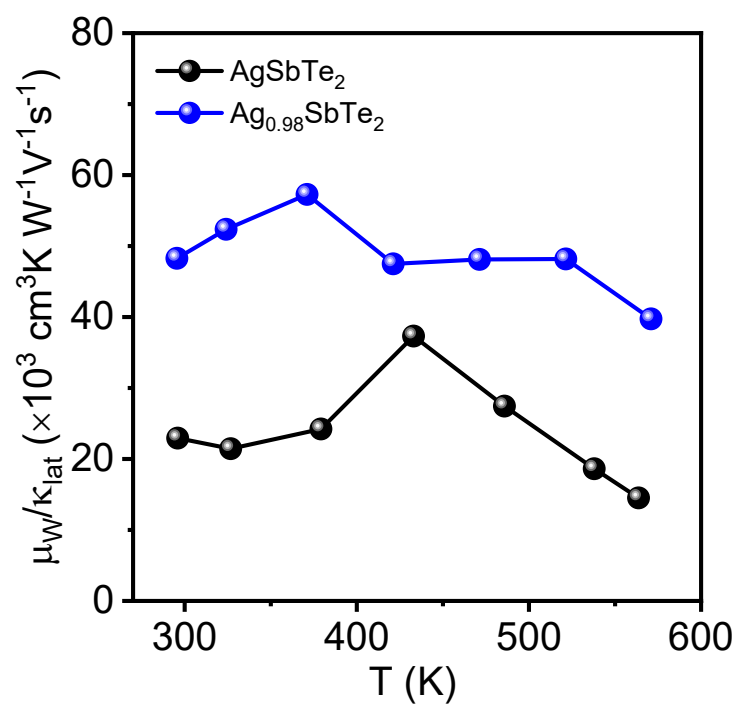
Fig. S12 Temperature dependence of μ_W/κ_{lat} of AgSbTe$_2$ and Ag$_{0.98}$SbTe$_2$.
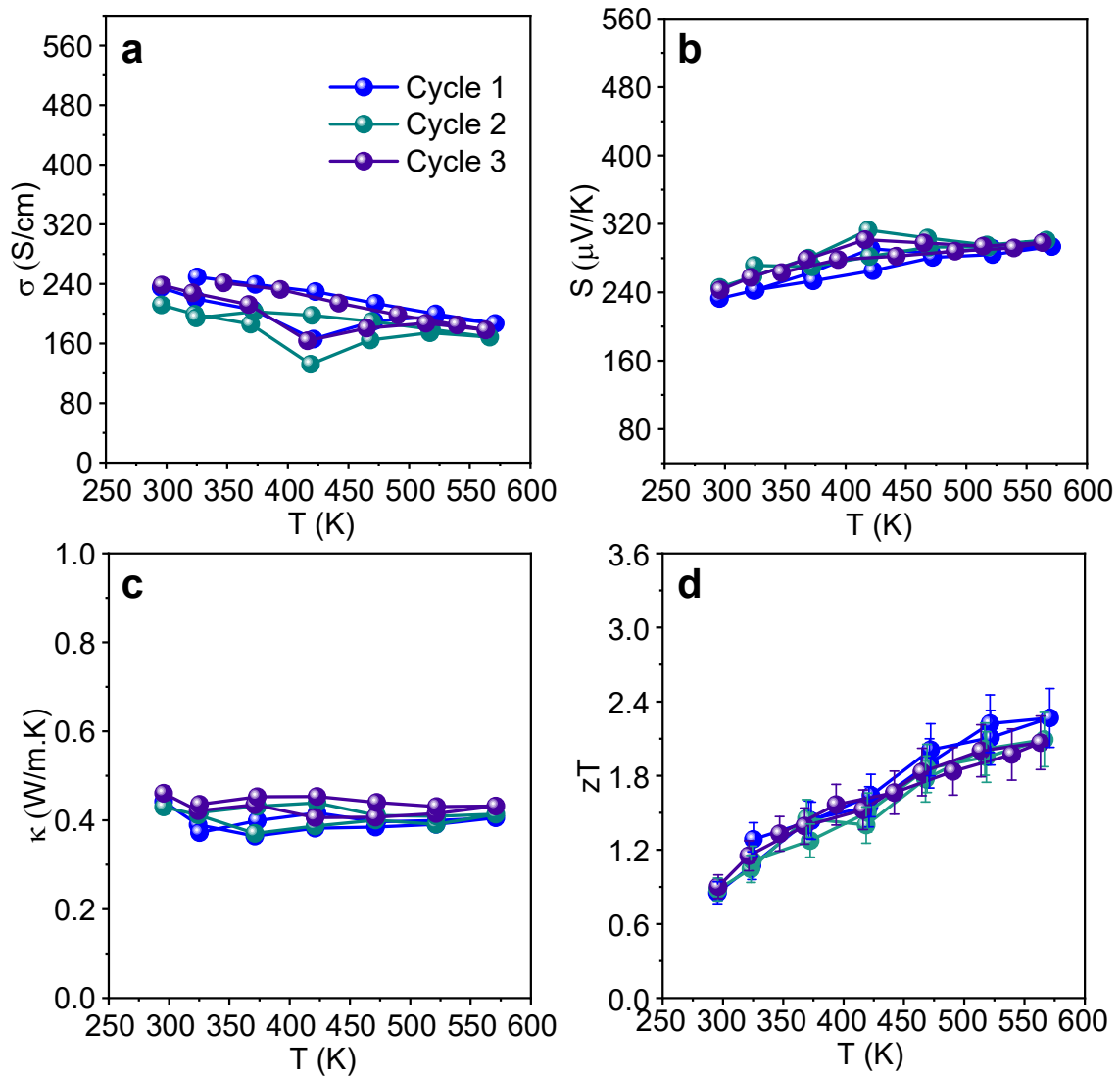
Fig. S13 Temperature variation of (a) electrical conductivity (σ), (b) Seebeck coefficient (*S*), (c) total thermal conductivity (κ_{tot}) and (d) thermoelectric figure of merit (zT) of $Ag_{0.98}SbTe_2$ (within error bar is ~15 %) for three consecutive heating-cooling cycles.
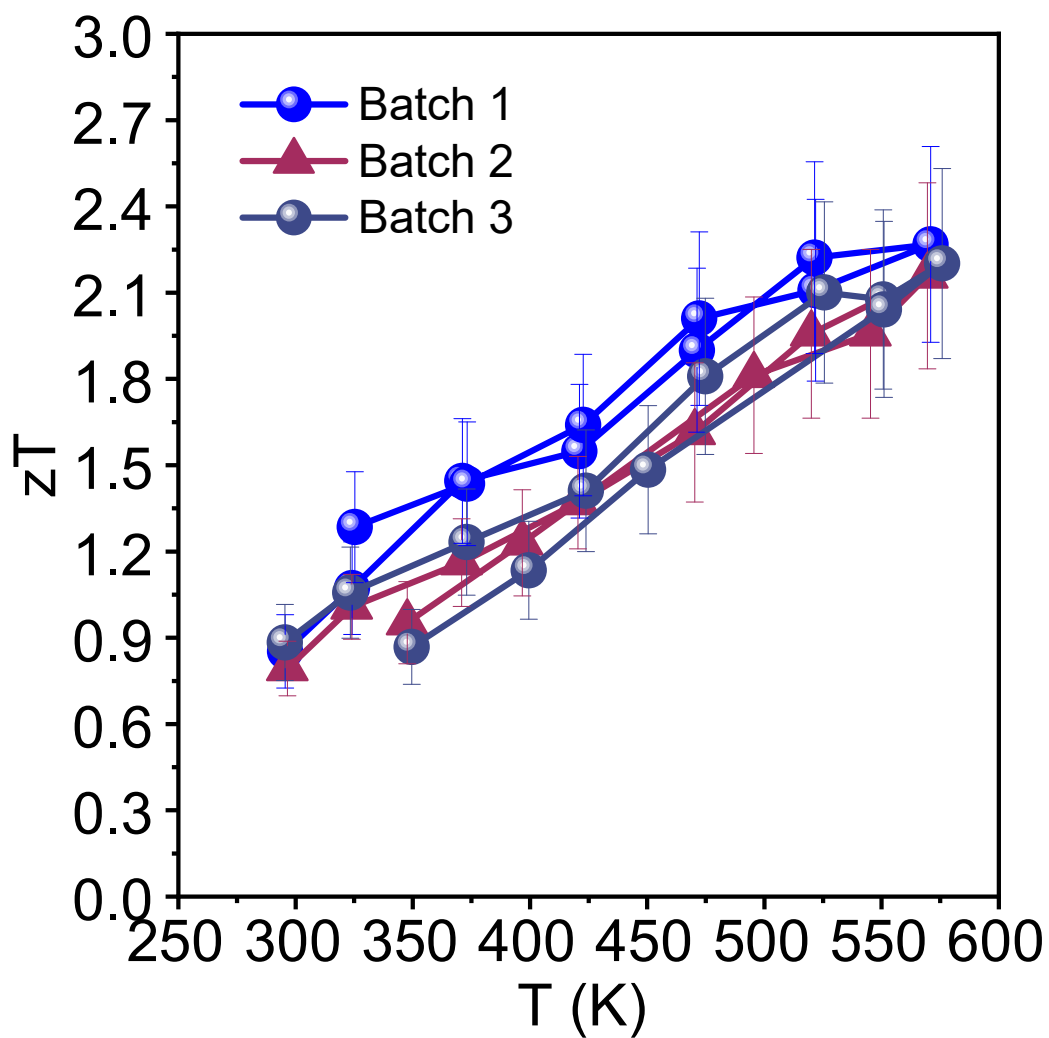
Fig. S14 Temperature variation of zT in three different batches of $Ag_{0.98}SbTe_2$ (The error bar is ~15%).
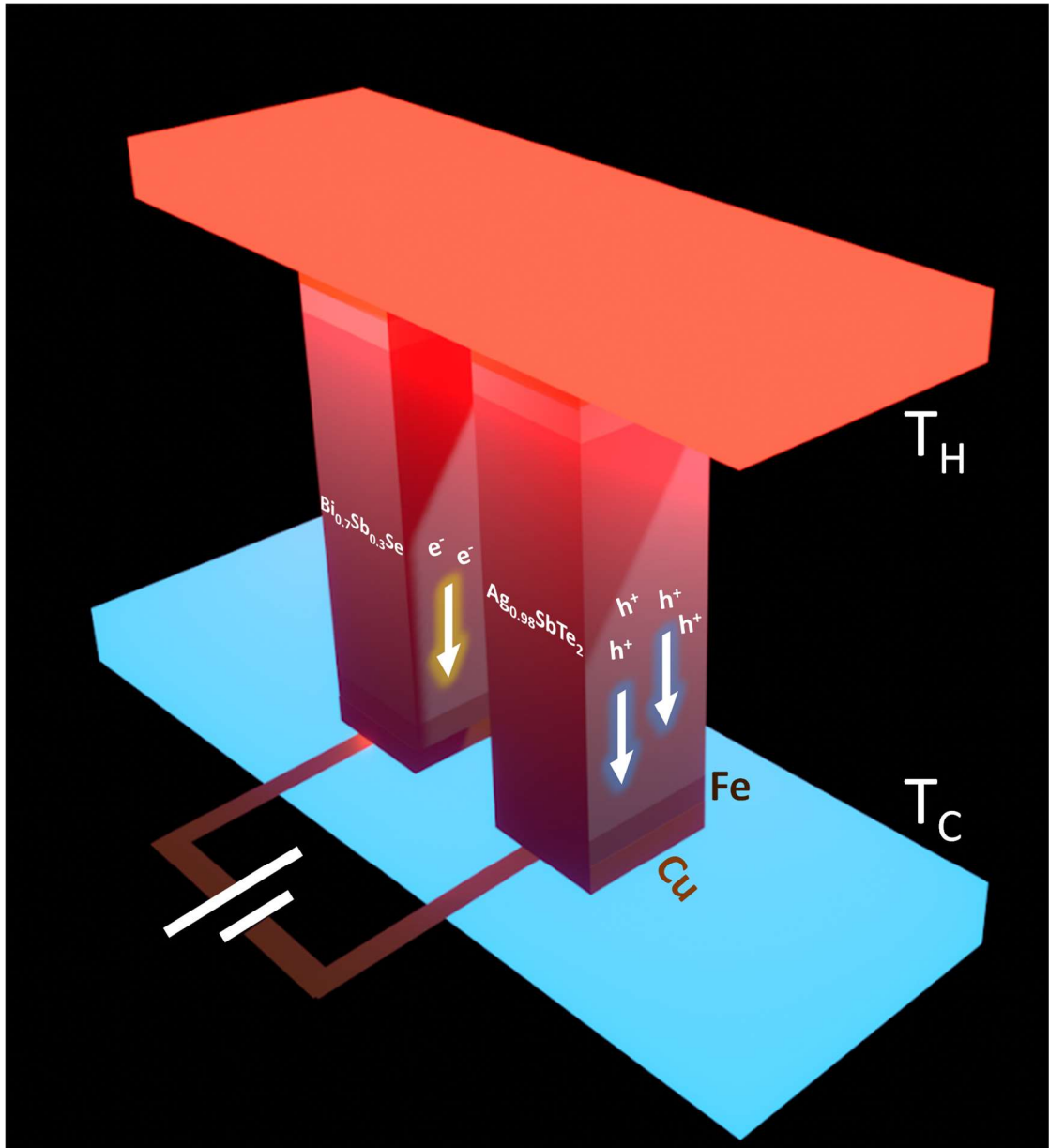
Fig. S15 Schematic of double-leg thermoelectric device based on $Ag_{0.98}SbTe_2$ showing all the parts.
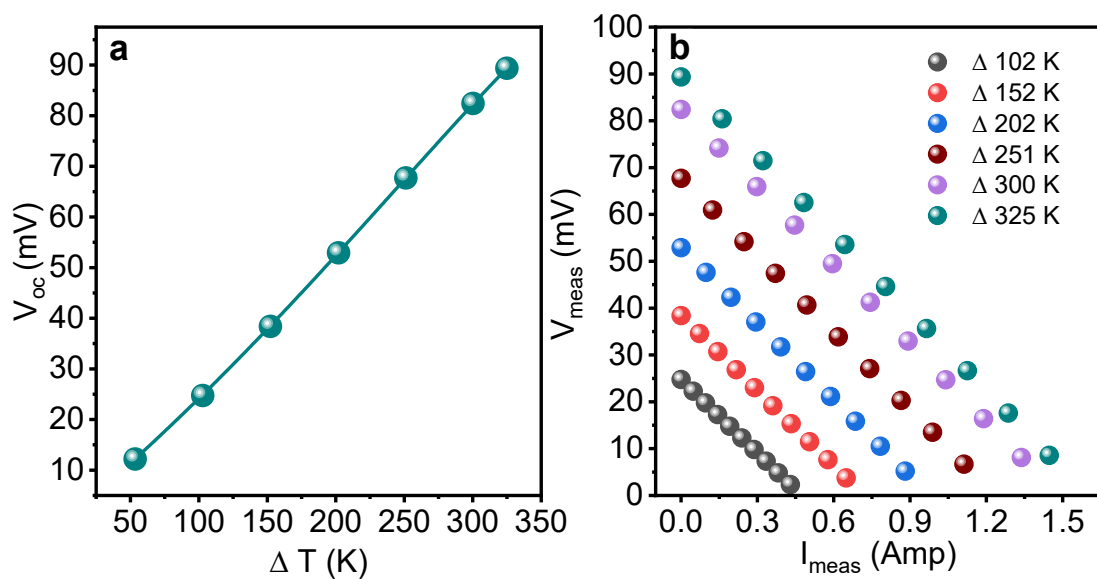
Fig. S16 (a)**,** Variation of open circuit voltage (V_{oc}) as a function of ΔT and (b) current dependent output voltage (V_{meas}) at different ΔT.
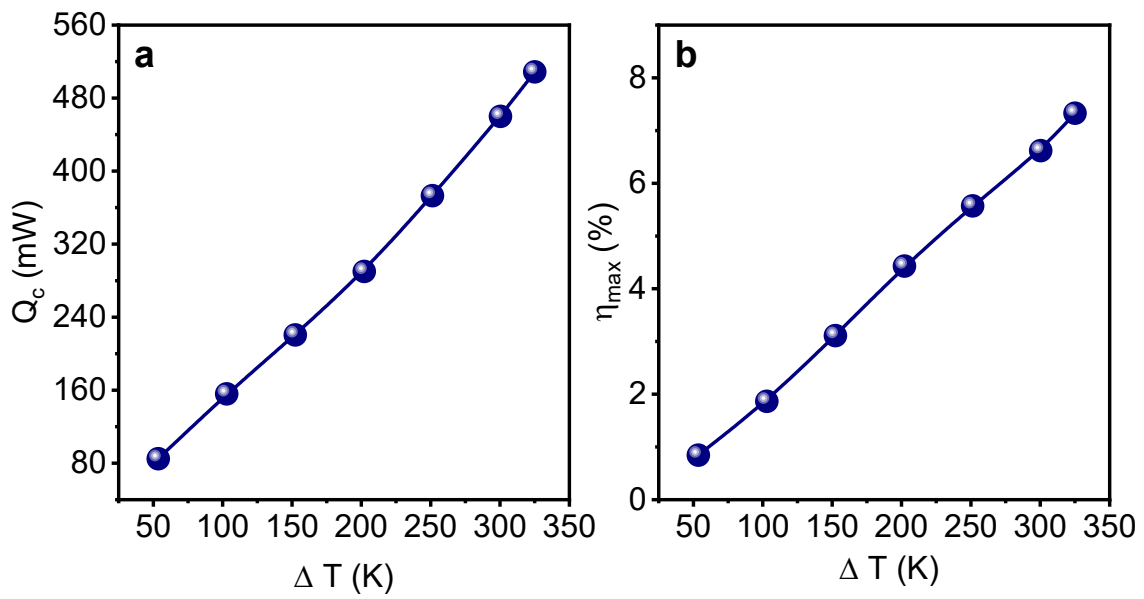
Fig. S17 Variation of (a) total amount of heat flow (Q_c) using the Fourier Law and (b) the maximum thermoelectric efficiency (η_{max}) as a function of ΔT of the fabricated double leg thermoelectric device.

Table S1. Fitting parameter of Positron annihilation lifetime plot.

Sample	τ_1 (ps)	I_1 (%)	τ_2 (ps)	I_2 (%)	τ_3 (ps)	I_3 (%)
$AgSbTe_2$	160	30	309	68	3089	1
$Ag_{0.98}SbTe_2$	165	28	314	71	3370	1
$Ag_{0.97}SbTe_2$	161	25	325	74	3645	1

Table S2. Experimental sound velocity of $Ag_{1-x}SbTe_2$ (x = 0, 0.01, 0.2, and 0.03)

Sample	Longitudinal Sound Velocity (v_l)	Transverse Sound Velocity (v_t)	Mean Sound Velocity (v_m)
$AgSbTe_2$	2758 m/s	1629 m/s	1804 m/s
$Ag_{0.99}SbTe_2$	2682 m/s	1567 m/s	1738 m/s
$Ag_{0.98}SbTe_2$	2475 m/s	1456 m/s	1613 m/s
$Ag_{0.97}SbTe_2$	2588 m/s	1569 m/s	1733 m/s

Table S3. Parameters obtained from the fitting of low-temperature C_p/T vs. T^2 data of AgSbTe$_2$ and Ag$_{0.98}$SbTe$_2$ using a Debye Einstein model.

Parameters	AgSbTe$_2$	Ag$_{0.98}$SbTe$_2$
γ	0.00515 J/mole.K^2	0.00817 J/mole.K^2
β	0.000202 J/mole.K^4	0.000351 J/mole.K^4
E1	30.1 K	28.8 K
E2	62.1 K	59.2 K
E3	119.1 K	114.4 K
Θ_D	164 K	154 K

References.

1. S. Roychowdhury, T. Ghosh, R. Arora, M. Samanta, L. Xie, N. K. Singh, A. Soni, J. He, U. V. Waghmare and K. Biswas, *Science*, 2021, **371**, 722-727.
2. D. G. Cahill, S. K. Watson and R. O. Pohl, *Phys. Rev. B*, 1992, **46**, 6131-6140.
3. M. T. Agne, R. Hanus and G. J. Snyder, *Energy Environ. Sci.*, 2018, **11**, 609-616.
4. V. Jovovic and J. P. Heremans, *Phys. Rev. B*, 2008, **77**, 245204.
5. R. Pathak, P. Dutta, A. Srivastava, D. Rawat, R. K. Gopal, A. K. Singh, A. Soni and K. Biswas, *Angew. Chem. Int. Ed.*, 2022, **61**, e202210783.
6. A. Sarkar, M. Chakrabarti, S. K. Ray, D. Bhowmick and D. Sanyal, *J. Phys.: Condens. Matter.*, 2011, **23**, 155801.
7. H. Luitel, A. Sarkar, M. Chakrabarti, S. Chattopadhyay, K. Asokan and D. Sanyal, *Nuclear Inst. and Methods in Physics Research, B: Beam Interactions with Materials and Atoms*, 2016, **379**, 215-218.
8. D. Sanyal, D. Banerjee, R. Bhattacharya, S. K. Patra, S. P. Chaudhuri, B. N. Ganguly and U. De, *J. Mater Sci.*, 1996, **31**, 3447-3451.
9. S. Roychowdhury, M. Samanta, S. Perumal and K. Biswas, *Chem. Mater.*, 2018, **30**, 5799-5813.
10. J. P. Perdew, K. Burke and M. Ernzerhof, *Phys. Rev. Lett.*, 1996, **77**, 3865-3868.
11. G. Kresse and J. Furthmüller, *Phys. Rev. B*, 1996, **54**, 11169-11186.
12. G. Kresse and D. Joubert, *Phys. Rev. B*, 1999, **59**, 1758-1775.
13. K. Hoang, S. D. Mahanti, J. R. Salvador and M. G. Kanatzidis, *Phys. Rev. Lett.*, 2007, **99**, 156403.
14. M. Samanta, K. Pal, P. Pal, U. V. Waghmare and K. Biswas, *J. Am. Chem. Soc.*, 2018, **140**, 5866-5872.
15. X. Hu, M. R. Barnett and A. Yamamoto, *J. Alloys Compd.*, 2015, **649**, 1060-1065.
16. R. Chetty, Y. Kikuchi, Y. Bouyrie, P. Jood, A. Yamamoto, K. Suekuni and M. Ohta, *J. Mater Chem. C.*, 2019, **7**, 5184-5192.